ADVANCED ELECTRONIC MATERIALS
www.advelectronicmat.de

Check for updates

# Tailoring the Switching Dynamics in Yttrium Oxide-Based RRAM Devices by Oxygen Engineering: From Digital to Multi-Level Quantization toward Analog Switching

*Stefan Petzold,* Eszter Piros,* Robert Eilhardt, Alexander Zintler, Tobias Vogel, Nico Kaiser, Aldin Radetinac, Philipp Komissinskiy, Eric Jalaguier, Emmanuel Nolot, Christelle Charpin-Nicolle, Christian Wenger, Leopoldo Molina-Luna, Enrique Miranda, and Lambert Alff*

**This work investigates the transition from digital to gradual or analog resistive switching in yttrium oxide-based resistive random-access memory devices. It is shown that this transition is determined by the amount of oxygen in the functional layer. A homogeneous reduction of the oxygen content not only reduces the electroforming voltage, allowing for forming-free devices, but also decreases the voltage operation window of switching, thereby reducing intra-device variability. The most important effect as the dielectric becomes substoichiometric by oxygen engineering is that more intermediate (quantized) conduction states are accessible. A key factor for this reproducibly controllable behavior is the reduced local heat dissipation in the filament region due to the increased thermal conductivity of the oxygen depleted layer. The improved accessibility of quantized resistance states results in a semi-gradual switching both for the set and reset processes, as strongly desired for multi-bit storage and for an accurate definition of the synaptic weights in neuromorphic systems. A theoretical model based on the physics of mesoscopic structures describing current transport through a nano-constriction including asymmetric potential drops at the electrodes and non-linear conductance quantization is provided. The results contribute to a deeper understanding on how to tailor materials properties for novel memristive functionalities.**

## 1. Introduction

Resistive random-access memory (RRAM) counts to the most promising emerging non-volatile memory technologies due to its simple metal–insulator–metal (MIM) structure. RRAM shows promising characteristics such as fast (<1 ns)[1] and low-power switching (1 pJ per bit),[2] high endurance (>$10^9$ cycles),[3] resilience toward ionizing radiation,[4] and excellent scaling capability down to below 10 nm.[5] Resistive switching has been observed in materials such as hafnium, tantalum, and yttrium oxide,[6–8] which are well-established materials in complementary metal oxide semiconductor (CMOS) technology, making RRAM easily integrable in existing back-end-of-line Si technology, and thus, an interesting candidate for new emerging applications such as cybersecurity and neuromorphic computation. In particular, neuromorphics is becoming increasingly important due to emerging fields like autonomous driving, image recognition, and deep learning. The

Dr. S. Petzold, E. Piros, T. Vogel, N. Kaiser, Dr. A. Radetinac,
Dr. P. Komissinskiy, Prof. L. Alff
Advanced Thin Film Technology Division
Institute of Materials Science
Technische Universität Darmstadt
Alarich-Weiss-Straße 2
64287, Darmstadt, Germany
E-mail: stefan.petzold@tu-darmstadt.de; eszter.piros@tu-darmstadt.de

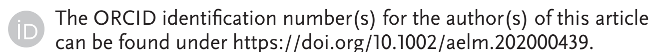
The ORCID identification number(s) for the author(s) of this article can be found under https://doi.org/10.1002/aelm.202000439.

© 2020 The Authors. Published by Wiley-VCH GmbH. This is an open access article under the terms of the Creative Commons Attribution License, which permits use, distribution and reproduction in any medium, provided the original work is properly cited.

DOI: 10.1002/aelm.202000439

R. Eilhardt, A. Zintler, Prof. L. Molina-Luna
Advanced Electron Microscopy Division
Institute of Materials Science
Technische Universität Darmstadt
Alarich-Weiss-Straße 2
64287, Darmstadt, Germany

E. Jalaguier, E. Nolot, C. Charpin-Nicolle
CEA-LETI
17 Avenue des Martyrs
38054, Grenoble, France

Prof. C. Wenger
IHP–Leibniz-Institut fuer innovative Mikroelektronik
15236 Frankfurt (Oder), and BTU Cottbus-Senftenberg
03046, Cottbus, Germany

Prof. E. Miranda
Departament d'Enginyeria Electrònica
Universitat Autònoma de Barcelona
08193-Cerdanyola del Valles
Barcelona, Spain

requirements for these data centric applications cannot be fulfilled by the standard von Neumann computing, thus, creating a market entrance niche for alternative technologies. For recent reviews on RRAMs see, for example, refs. [6,9–13] and the references therein.

In the case of neuromorphic computing, highly parallelized and interconnected RRAM devices act as a network of electrical synapses, mimicking the behavior of the human brain. The learning behavior is represented by the analog change of synaptic weights due to electronic stimuli which can be reproduced by the resistance modulation in resistive switching devices. In valence change memory, the information storage relies on the formation and rupture of conducting filaments formed of oxygen vacancies. When the filament connects both electrodes, the device is in the low resistive state (LRS), whereas when the filament is ruptured, the high resistive state (HRS) is obtained. The exact mechanisms, role of interfaces and nature of the conducting filament is still under debate.[14–17]

When the size of the conducting filament reduces to the atomic scale, eventually conductance quantization phenomena may be observed even at room temperature. The quantum conductance unit is defined as $G_0 = 2e^2/h$,[18] where $e$ is the electron charge and $h$ the Planck constant, and equals 77 µS or $(12.9\ \text{k}\Omega)^{-1}$. Experimentally, integer and half-integer multiples of $G_0$ have been occasionally found.[19–24] In this paper, we suggest using these quantum states as a quasi-continuous reservoir of resistive states for analog switching. The key challenge so far is the volatility and fragility of these quantized states, and their occurrence predominantly in the reset, but not in the set process. An ideal neuromorphic system, however, would need to provide a high density of resistance states accessible in an analog manner in the set as well as in the reset operation.[24]

Gradual resistance switching is currently investigated in almost all materials systems which are candidates for non-volatile digital memory leading to a variety of proposed methods for controlling a transition from digital to analog switching.[25–28] Recently, $Y_2O_3$ has been suggested as a well-suited material for RRAM applications due to its intrinsic anion sublattice defect structure.[7] 1D oxygen vacancy chains along the [110] directions which form within its cubic structure, were proposed to act as quantum channels associated with gradual switching and forming-free devices.[7,29,30]

In this study, we show that the device behavior can be tuned from digital to multi-step toward a fully analog/gradual resistive switching behavior with a high number of quantized levels both in the set and reset processes by engineering of the oxygen content. Furthermore, we propose a physics-based model to account for the observed linear and nonlinear conductance quantization via the generalization of conduction through a quantum point contact with asymmetrical potential drops at the two ends of the nano-constriction. Simulations based on the proposed model reproduce the experimental current–voltage characteristics in the HRS and at intermediate resistive states with realistic materials and device parameters.

## 2. Oxygen Engineering of Devices

Yttrium oxide layers with varying oxygen content were achieved by oxygen engineering utilizing a custom designed reactive molecular beam epitaxy unit. By varying the oxygen flow through a radical source and (in case of the sample grown at 1.0 square cubic centimeter per minute (sccm)) by varying the growth rate, fine control of the oxygen content within the deposited layer was achieved. The growth conditions were optimized on test yttria films deposited on $c$-cut sapphire substrates. The $2\theta$-$\theta$ X-ray diffraction (XRD) patterns of these test samples are depicted in **Figure 1**a. For the films grown at

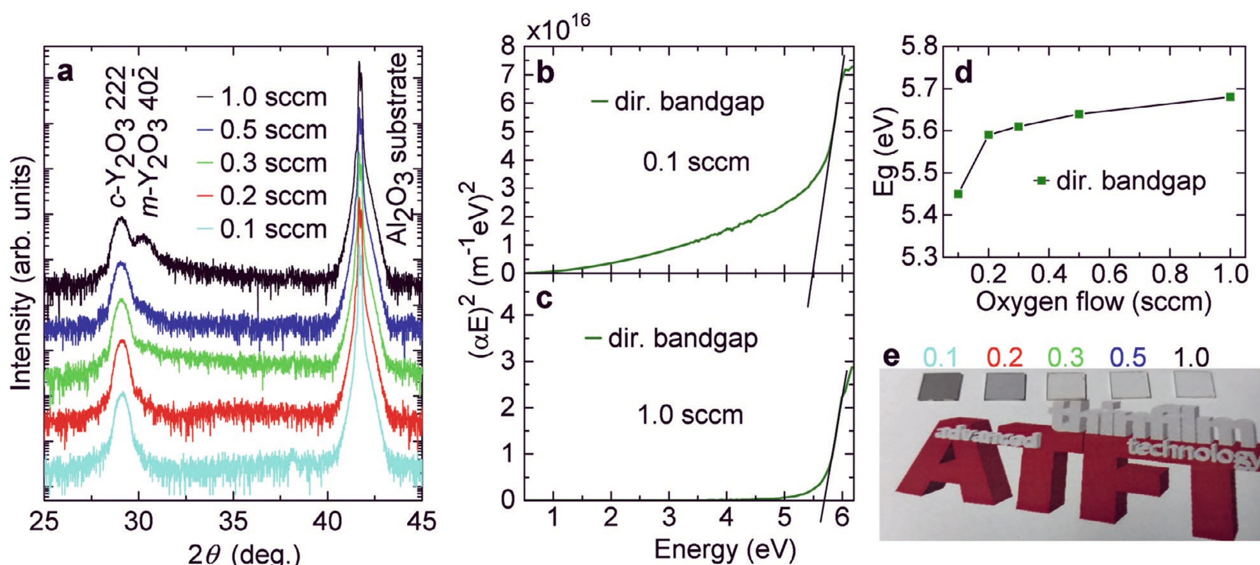


**Figure 1.** a) X-ray diffraction patterns for the test $YO_x$ layers grown on $c$-cut $Al_2O_3$ substrates at varied oxygen flow from 0.1 up to 1.0 sccm. b,c) Tauc plots of UV/vis transmission measurements for the yttria layers grown at the least (0.1 sccm) and highest (1.0 sccm) oxidation conditions, respectively. d) Direct bandgap of the yttria layers as a function of oxygen flow during their growth. The line only acts as a guide to the eye. e) Photograph of the five different yttria layers grown at varied oxygen flow from 0.1 up to 1.0 sccm.


© 2020 The Authors. Published by Wiley-VCH GmbH

**Table 1.** Overview table of growth parameter and characteristic values of the investigated $YO_x$ layers grown on top of the Si/Al/TiN structures.

| Growth | | XRR | UV/vis | XPS | | | |
|---|---|---|---|---|---|---|---|
| Oxygen flow [sccm] | Growth rate [Å $s^{-1}$] | Thickness [nm] | dir. $E_g$ [eV] | Y [%] | O [%] | (ii) Y-OH [%] | Metallic Y [%] |
| 0.1 | 1 | 18.88 | 5.45 | 44.5 | 55.5 | 16.9 | 12.4 |
| 0.2 | 1 | 16.81 | 5.59 | 45.7 | 54.3 | 18.4 | 1.2 |
| 0.3 | 1 | 15.85 | 5.61 | 39.4 | 60.6 | 22.6 | 0.4 |
| 0.5 | 1 | 14.95 | 5.64 | 39.4 | 60.6 | 23.8 | 0.3 |
| 1.0 | 0.25 | 13.19 | 5.68 | 39.6 | 60.4 | 23.3 | 0.3 |

low oxidation conditions (red and cyan curves, films grown at 0.1 and 0.2 sccm), the presence of only one cubic yttria (222) growth orientation in the XRD patterns indicates its highly textured growth. For higher oxidation conditions (a flow of 0.3 sccm and higher), an additional shoulder appears at higher $2\theta$ values at ≈30.3°, which is assigned to the $40\overline{2}$ reflection of a monoclinic phase of yttria. Note that the monoclinic phase (B-monoclinic—C2/m) of bulk yttrium oxide is only stable at high pressure of ≈10 GPa. However, it was recently demonstrated that the monoclinic phase can also be stabilized in yttria thin films at higher oxidation conditions.[31,32] Thus, the appearance of the $40\overline{2}$ monoclinic reflection in the XRD patterns of the samples grown at high oxygen flow indicates their full oxygen stoichiometry.

Tauc plots resulting from UV/vis transmission measurements for the least (an oxygen flow of 0.1 sccm) and most oxidized (1.0 sccm) yttria layers are depicted in Figure 1b,c, respectively. The direct optical bandgaps of all grown test yttria samples were extracted via extrapolation assuming parabolic valance and are plotted in Figure 1d as a function of oxygen flow, showing a decrease of the bandgap with decreasing oxygen content of the $YO_x$ films. Over the oxygen content series, the direct bandgap decreases from 5.7 eV by over 0.2 eV to 5.45 eV. The precise values are given in **Table 1** and correspond well to the bandgap values previously reported in the literature for yttrium oxide.[33] At the same time, the overall transmission drastically decreases at low oxidation conditions (e.g., from 100% down to 60% at 1000 nm wavelength). This effect of oxygen engineering is also observable in the optical images of the test yttria samples in Figure 1e. The samples with the yttria layers grown with high oxygen flow (1.0–0.3 sccm) are transparent to the eye, while the samples with oxygen deficient yttria films are grayish and opaque. Note that the yttria bandgap and optical transparency of the samples change considerably with the decrease of oxygen flow from 0.3 to 0.2 sccm, that is, upon the disappearance of the monoclinic reflection in Figure 1a. The reason hereof is related to an increased density of defects (oxygen vacancies) in oxygen deficient yttria, which act as scattering centers for photons and reduce the overall intensity of the transmitted optical signal.

The thickness of the yttria layers is ≈15 nm and increases for oxygen deficient samples. The exact thickness values have been derived from the period of the measured X-ray reflectometry (XRR) oscillations (see Figure S1, Supporting Information), using an RCRefSim software[34] and are summarized in Table 1. The XRR data also reveal undamped oscillations up to angles of more than 6° proving low interface and surface roughness. The critical angle of the XRR (see the inset of Figure S1, Supporting Information) reduces continuously with decreasing oxidation conditions implying an increase in electron density for less oxidized yttria films.

The growth of the yttria layers for the RRAM devices was performed under the same deposition conditions as demonstrated previously on *c*-cut sapphire. The MIM thin-film structures of an Al/TiN/$YO_x$/Pt configuration were produced on Si substrates. First, an Al buffer layer and TiN bottom electrode (BE) were grown on a (100) Si substrate by atomic layer deposition (ALD). The platinum top electrode (TE) was deposited by DC-sputtering ex situ after the XRD measurements of the Si/Al/TiN/$YO_x$ stacks. The recorded XRD patterns of the fabricated stacks are depicted in **Figure 2**a. The aluminum and TiN layers predominantly show a (111) orientation. Similar to the growth on *c*-cut sapphire, the yttria layers show reflections from the monoclinic and cubic phases. For all growth conditions, the 222 and 332 reflections from the cubic phase are observed in Figure 2a. For the growth with an oxygen flow equal or higher than 0.3 sccm, the $40\overline{2}$ reflection from the monoclinic phase of yttria is detectable resulting in a decrease of both the 222 and 332 cubic reflections. By reducing the oxidation conditions, the monoclinic phase can be suppressed, allowing for the fabrication of phase-pure cubic yttria. This is of utmost importance as will be discussed later in connection with the forming voltages.

To give a deeper insight into crystallinity and stoichiometry of the yttria films, annular bright field (ABF) scanning transmission electron microscopy (STEM) images of the stacks cross-sections have been acquired. Electron energy loss spectra (EELS) of the oxygen K-edge for the yttria layers grown with an oxygen flow of 1.0 and 0.1 sccm are shown in Figure 2b. The ABF-STEM images for the yttria layers of the same stacks are shown in Figure 2c,d, respectively. To correlate the ABF-STEM images with the orientations of yttria grains, multislice simulation images generated using the Dr. Probe[35] software were overlaid on selected magnified areas of the ABF-STEM images (see Figure 2e,–g). The stoichiometric yttria stack shows mixed cubic (332) and monoclinic ($40\overline{2}$) oriented grains and the deficient yttria stack shows a ($10\overline{3}$) oriented cubic phase. The observation of a purely cubic phase in the oxygen deficient yttria layer is consistent with the changes observed in the XRD patterns. The ($10\overline{3}$) orientation, as shown by the ABF-STEM images, resembles a forbidden reflection in XRD and is therefore not visible in the XRD pattern. The influence of stoichiometry is also present in the EEL spectra: with increasing number of oxygen vacancies with decreasing oxygen flow, the intensity ratio of the two major yttria peaks is altered, and they are shifted toward lower energy values, namely, from 533.8 and

 © 2020 The Authors. Published by Wiley-VCH GmbH

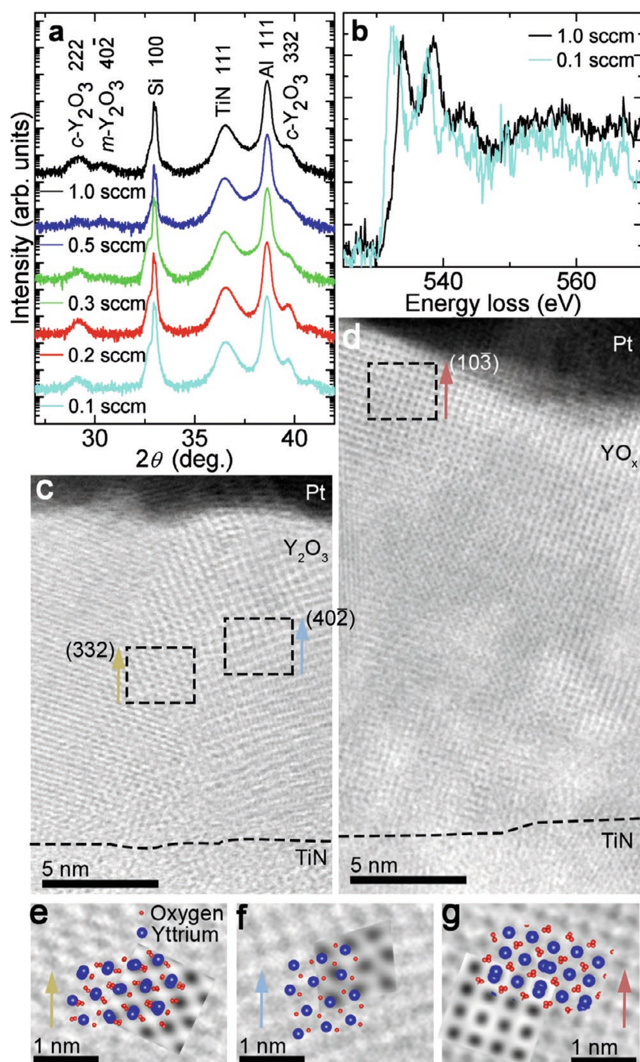


**Figure 2.** a) XRD patterns of the Si/Al/TiN/$YO_x$ stacks. The growth conditions of the yttria layers are the same as for the previously discussed layers on *c*-cut sapphire. b) EEL spectra of the O K-edge for the $YO_x$ layers grown with oxygen flow of 1.0 sccm (black) and 0.1 sccm (cyan). The background spectra have been subtracted. ABF-STEM images of the stacks with the c) highest and d) lowest oxidation conditions. e–g) Multislice simulations were used to determine the growth orientations of the individual grains, here magnified views of the marked regions in (c) and (d) are shown. For the film grown at the highest oxidation condition (1.0 sccm), a growth orientation of e) cubic (332) and f) monoclinic (40$\bar{2}$) is observed (projected along (1$\bar{1}$0) and (010), respectively). g) For the lowest oxidation condition (0.1 sccm), cubic (10$\bar{3}$) is observed as grain growth orientation (projected along (1$\bar{1}$0) in the micrograph).

538.5 eV to 532.6 and 537.5 eV for the films grown with 1.0 and 0.1 sccm, respectively.[36]

The results of the X-ray photoelectron spectroscopy (XPS) measurements of the yttria layers grown on Si/Al/TiN are depicted in **Figure 3**. For all films, the Y3d spectra show a $Y3d_{5/2}$ and $Y3d_{3/2}$ multiplet due to spin–orbit coupling. For the film grown with the lowest oxygen flow of 0.1 sccm, an additional emission of metallic yttrium is visible at low binding energies at 156.5 eV (Figure 3a). The O1s spectra for all yttria layers

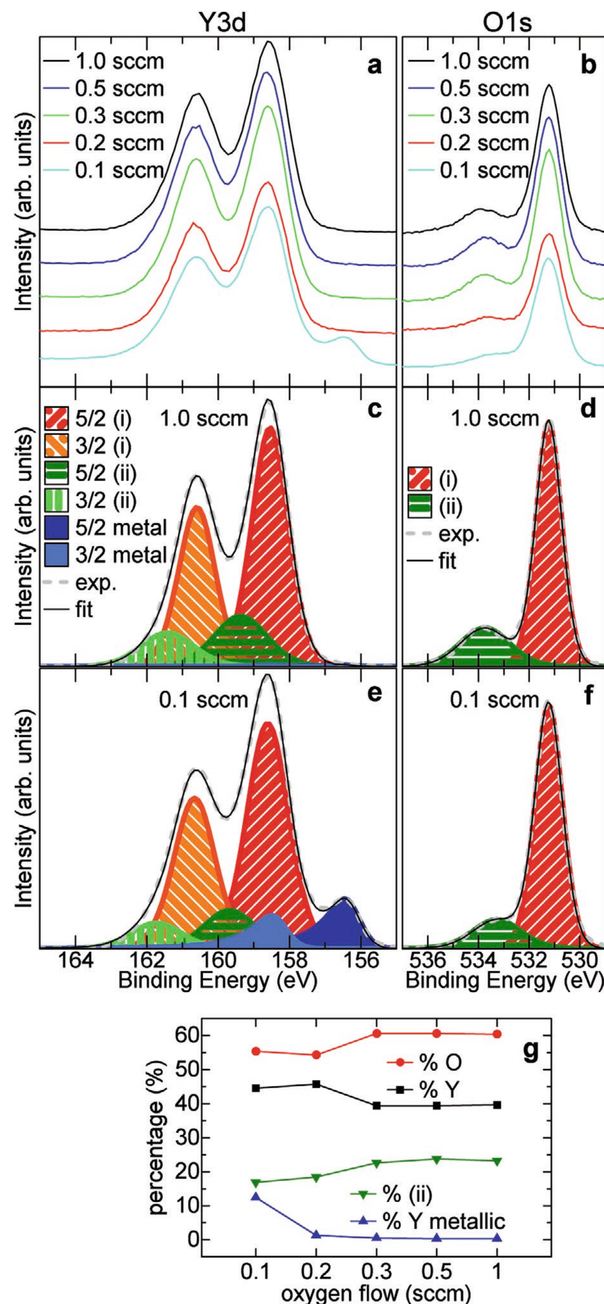


**Figure 3.** X-ray photoelectron spectroscopy of the $YO_x$ layers grown on Si(100)/Al/TiN. a) Measured Y3d and b) O1s spectra of the $YO_x$ layers grown under varied oxidation conditions, respectively. c–f Measured Y3d and O1s spectra with corresponding fits for the $YO_x$ layers grown with the oxygen flow of c,d) 1.0 sccm and e,f) 0.1 sccm, respectively. Y3d and O1s emissions from two different $YO_x$ phases denoted as (i) and (ii) are used to fit the experimental spectra. A 3d emission from metallic yttrium in the layer grown with oxygen flow of 0.1 sccm is depicted in blue. g) Summarized evaluation results of the XPS measurements. The yttrium to oxygen ratio decreases from 45:55 to 40:60 with increasing oxidation condition. At the same time, the metallic fraction of the yttrium species reduces from 12% (for 0.1 sccm) to about 0% (for 1.0 sccm of oxygen flow). The ratio of the peaks representing (i) and (ii) increases with increasing oxygen content. Note that the lines in the plot only act as a guide to the eye. For the origin of the (i) and (ii) contributions, please refer to the discussion in the main text.


© 2020 The Authors. Published by Wiley-VCH GmbH

ADVANCED ELECTRONIC MATERIALS
www.advelectronicmat.de

show two distinctive peaks at ≈531 and 534 eV (Figure 3b). All spectra have been aligned to the Fermi level attributed to the metallic states in the bandgap of the least oxidized yttria layer. The valence band spectra recorded for all layers are depicted in Figure S2, Supporting Information.

For the $YO_x$ layers grown with the oxygen flow of 0.2–1.0 sccm, excellent fits of the experimental Y3d spectra have been done, using two Y3d components denoted as (i) and (ii) in Figure 3c,e. The $Y3d_{5/2}$ ($Y3d_{3/2}$) emissions are obtained at the binding energies of 158.5 eV (160.6 eV) and 159.5 eV (161.6 eV) for the (i) and (ii) components, respectively. A constant energy difference between the $Y3d_{5/2}$ and $Y3d_{3/2}$ emissions of 2.1 eV is observed. During the fitting, the ratio between the intensities of $Y3d_{5/2}$ and $Y3d_{3/2}$ has been fixed to 3:2 for both the (i) and (ii) components in a good agreement with the experimental data. For the most oxygen deficient yttria layer (oxygen flow of 0.1 sccm), the positions of the $Y3d_{5/2}$ and $Y3d_{3/2}$ emissions for the (i) and (ii) are shifted by 0.2 eV toward higher binding energies. The chemical shift between the components (i) and (ii) is therefore about 1.2 eV for the least oxidized layer (0.1 sccm) and about 1.0 eV for all layers grown at higher oxygen flows. In order to fit the experimental Y3d spectrum for the least oxidized yttria layer (oxygen flow of 0.1 sccm), an additional spectral contribution for metallic yttrium with the energies of 156.4 and 158.5 eV for the $Y3d_{5/2}$ and $Y3d_{3/2}$ emissions, respectively,[37,38] is required to give a good fit to the experimental data (bluish areas in Figure 3c).

Two peaks, (i) and (ii), are also necessary for fitting the O1s spectra (Figure 3d,f). With an increase of the oxygen flow, peak (i) remains constant at a binding energy of 531.2 eV. However, the peak (ii) is shifted by 0.5 eV from 533.2 (0.1 sccm) to 533.7 eV (1.0 sccm). For this reason, the chemical shift between the (i) and (ii) O1s components increases from 2.0 to 2.5 eV with increasing oxidation conditions.

For each yttria layer, the ratio between the (i) and (ii) spectral components of Y3d and O1s is congruent and the weight of the (ii) component increases with oxygen flow. The fitted XPS spectra for all grown $YO_x$ layers are available in Figure S3, Supporting Information. The extracted (i) and (ii) spectral components might originate from two different chemical environments of Y and O atoms, namely

1. a differing coordination between yttrium and oxygen due to two possible nonequivalent positions of yttrium on the cation sublattice,[39]
2. a reaction with hydrogen or water resulting in hydroxide formation at the surface (Y–OH).[31,40,41]

Yttrium oxide is known to have a defective structure with defects in the anion lattice, and thus, has two preferred coordinations with oxygen. Nevertheless, the chemical shift of 1.0 eV seems too large for this scenario. Taking the highly hydrophilic character of yttrium oxide into account, the emerging (ii) component is most likely related to the second case, namely a surface reaction with residual water in the vacuum chamber resulting in hydroxide formation at the sample surface prior to the XPS measurements. This scenario is also supported by the fact that XPS measurements at lower angles are more surface sensitive and show higher fraction of the Y–OH contribution (ii). Additionally, the easy formation of hydroxide at the $YO_x$ surface is in qualitative agreement with the electronegativity (EN) of the involved species ($H_{EN}$ of 2.2, $Y_{EN}$ of 1.22, and $O_{EN}$ of 3.44) and the direction of the observed chemical shifts. Note that the shift of contribution (ii) to higher binding energies under less oxidizing conditions implies that there are no other valence states between the +3 and the metallic state for yttrium oxide. Therefore, the results underline, that although the oxygen content has been tuned in a wide range, the only stable valence state for yttrium remains +3.

Analyzing the fitted XPS spectra, the fraction of oxygen, yttrium, metallic yttrium, and of the (ii) component which is attributed to Y–OH, can be extracted, taking relative sensitivity factors of 23.27 for yttrium and 7.309 for oxygen into account. The results are depicted in Figure 3g, stating an increase of relative concentrations of oxygen and Y–OH (the (ii) spectral component) with increasing oxidation conditions, while the fraction of yttrium and metallic yttrium is decreasing.

Note that through oxygen engineering, we were able to grow and stabilize highly substoichiometric films with a metallic fraction of yttrium as high as 12.4% and a ratio of yttrium to oxygen of $Y_{0.45}O_{0.55}$. The composition of the investigated $YO_x$ layers, extracted from the XPS analysis, is summarized in Table 1.

To summarize so far, by means of oxygen engineering we were able to manipulate the optical appearance of the grown $YO_x$ layers and to decrease their direct optical bandgap by about 0.25 eV. By choosing low oxidation conditions, the purely cubic phase of yttrium oxide could be fabricated and the monoclinic phase was suppressed, resulting in highly oxygen deficient yttria films with electronic states in the bandgap, a metallic fraction as high as 12.4%, and a stoichiometry of $Y_{0.45}O_{0.55}$.

In the following, we demonstrate the beneficial effect of oxygen engineering on the resistive switching performance and enhanced accessibility of quantized conductance states of yttrium oxide-based RRAM.

## 3. Electrical Characterization

First, for each oxidation condition, an electroforming step was performed for 50 RRAM devices by applying voltage to the Pt top electrode with the TiN bottom electrode grounded. The forming voltage distributions are depicted in **Figure 4**a in the form of box plots. A clear trend consisting in a reduction of the forming voltages with decreasing oxygen flow can be identified. The average forming voltage for devices grown with 1.0 sccm of oxygen is about 6 V and can be tuned down to 1.4 V by reducing the oxidation conditions (0.1 sccm), rendering forming-free devices. The constitutional oxygen vacancy chains present in the cubic phase of yttria can serve as low energy migration paths for oxygen ions and hence promote filament formation.[29,42] With respect to the film orientation, these chains are oriented at rather small angles, thus, it is possible that they can intersect the whole film, and so aid the lowering of forming voltages. In the most oxidized stacks (1.0—0.3 sccm), however, the presence of the monoclinic phase, which lacks the constitutional vacancies, might result in the observed higher voltage values with respect to the oxygen deficient films. Also, according to Zheng et al.,[43] the native point defects


© 2020 The Authors. Published by Wiley-VCH GmbH

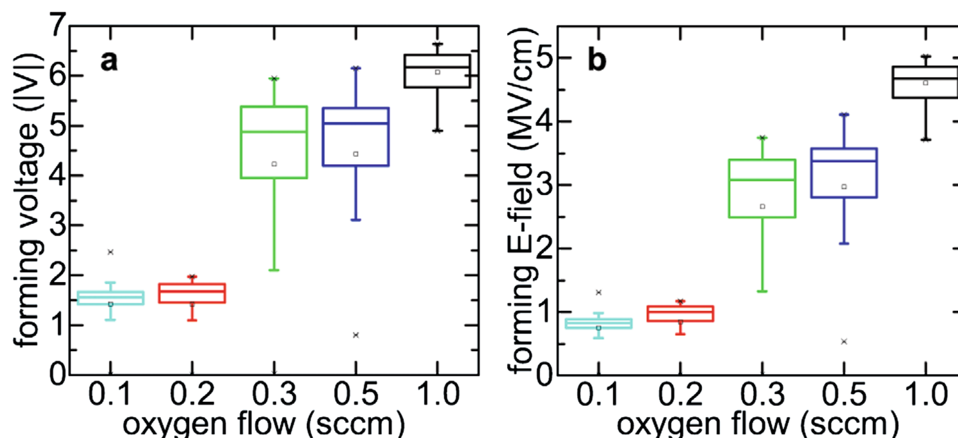


**Figure 4.** a) Box plot representation of the forming voltage distribution for yttrium oxide layers grown with different oxygen flow (0.1–1.0 sccm). For each oxidation condition, 50 devices have been evaluated. The trend proves that oxygen engineering can be utilized to reduce the forming voltage to the point of forming-free behavior. b) Box plots of the electric field necessary for soft breakdown (forming) of 50 RRAM devices. Taking the different yttrium oxide thicknesses into account, the trend of reducing forming voltages with decreasing oxygen content becomes more pronounced.

under high oxygen chemical potential in cubic, perfect yttrium oxide are oxygen interstitials, whereas at low oxygen chemical potential the stable defects are oxygen vacancies. In accordance with this, via oxygen engineering it is possible to control the oxygen chemical potential: in the samples with high oxygen content, the oxygen interstitials can hinder the electroforming and switching process, while via decreasing the oxygen content, the interstitials become unstable while the formation energy of oxygen vacancies is reduced and energetically preferred, which results in the observed low forming voltages.

Considering the gradient of the oxide thicknesses, the trend in the electroforming process becomes more pronounced by plotting the data in terms of the electric field (see Figure 4b). The electric field required for the soft dielectric breakdown of the yttria layer reduces from 5 MV cm$^{-1}$ (1.0 sccm) to below 1 MV cm$^{-1}$ (0.1 sccm). Therefore, oxygen engineering allows to access higher oxide thickness for RRAM devices in CMOS technology while satisfying its low operation voltage regime. By increasing the oxide thickness, and thus, the material reservoir of the functional switching layer, the RRAM endurance can be enhanced.[44]

Amongst the investigated devices, the samples grown with 0.3 sccm show the highest distribution of forming voltages. A possible reason for this might be that the devices in question are on the boundary of eliminating the monoclinic phase. Presumably because of the presence of the monoclinic structure, the mean value of the electroforming voltage is still clearly higher than the films with lower oxygen content. However, given the device size of 30 × 30 µm$^2$ and the polycrystalline structure of the yttria layer, it is possible that the low-energy path of electron transport in some of the devices in question was through purely cubic grains in the oxide (or where the monoclinic contribution is negligible), therefore resulting in the occasional occurrence of lower forming voltages. Additionally, randomly organized networks of grain boundaries have been identified as an additional source for forming voltage variation.[45] Recently, we have demonstrated how this disadvantage can be utilized via grain boundary engineering to even improve the forming voltage distribution.[46] Overall, a relatively higher distribution of $V_{forming}$ in the 0.3 sccm devices when compared to the other oxygen flows does not influence the general trend of the forming voltage scaling with oxygen content.

The effect of oxygen engineering on the resistive switching behavior is depicted in **Figure 5**. Figure 5b,d,f,h,j shows switching curves for the whole *I*–*V* range of DC operation. The reset operation is carried out in the positive voltage direction (applied to the Pt TE) which represents a movement of oxygen ions toward the Pt interface. Stable bipolar resistive switching can be achieved with the set process under negative bias due to the different work function of the top and bottom electrodes.[47] As the set operation is carried out in the negative voltage polarity, it results in the storage of oxygen in the TiN bottom electrode,[48] later acting as an oxygen reservoir for the reset process.

The following trends can be observed in the resistive switching properties with decreasing oxygen content (decreasing oxygen flow) of the functional yttrium oxide layer:

- set operation voltages and their variability decrease,
- set and reset processes show an increasing number of intermediate resistance states which are partly quantized,
  - reset process changes from digital to gradual,
  - set process changes from digital to stepwise with an increased number of quantized intermediate resistance states,
- onset of reset voltages increases, while the maximum applied reset voltages decrease,
- the resistance level of the HRS decreases while the LRS level remains unaltered.

As can be seen from the *I*–*V* characteristics of the different yttrium oxide layers, the voltage necessary to induce a set operation reduces with decreasing oxygen content of the yttrium oxide layers (similar to the trend of forming voltages in Figure 4). For all devices, the set voltage is defined as the voltage where the difference between two consecutive current measurement points is the highest. The detailed set voltage statistics for the different oxygen contents are summarized as box plots in **Figure 6**b. This reduction in operation voltage is


© 2020 The Authors. Published by Wiley-VCH GmbH

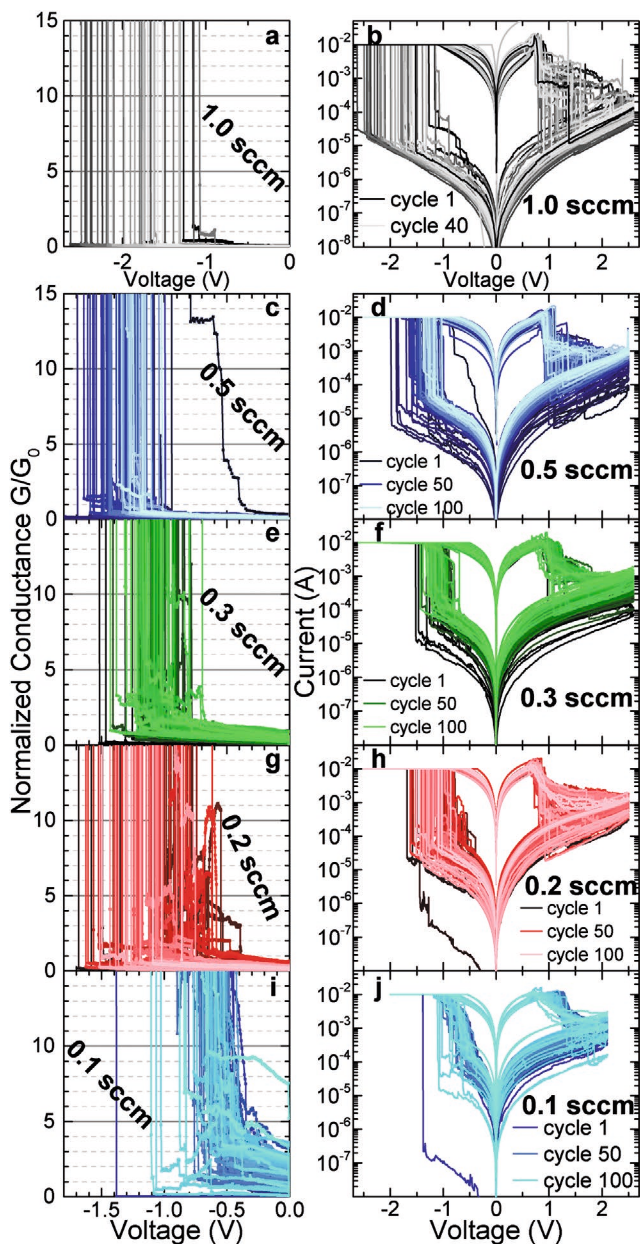


**Figure 5.** *I–V* curves of bipolar resistive switching behavior of yttrium oxide-based RRAM devices grown with varying oxygen flow of b) 1.0 sccm, d) 0.5 sccm, f) 0.3 sccm, h) 0.2 sccm, j) 0.1 sccm. While the set process takes place in the negative voltage direction, the reset process occurs in the positive voltage direction (Pt TE biased, while TiN BE is grounded). With decreasing oxidation conditions, both the set and reset processes show more intermediate, quantized conductance steps until finally showing gradual-like behavior. The quantized conductance states become apparent by plotting the conductance of the devices normalized by the quantum conductance $G_0$ for the set process as depicted for the different yttrium oxide-based devices grown at different oxygen flow of a) 1.0 sccm, c) 0.5 sccm, e) 0.3 sccm, g) 0.2 sccm, i) 0.1 sccm. Additionally, with decreasing oxygen flow, the set operation voltages decrease, and the high resistive state levels are decreasing in resistance while the onset of reset voltages increase slightly.

accompanied by additional, intermediate resistance states in the set operation which reproducibly show quantized conductance levels becoming more apparent with lower oxygen content of the yttrium oxide films. This behavior is highlighted in Figure 5a,c,e,g,i, where the conductance is normalized by the quantum conductance unit ($G_0$ = (12.9 kΩ)$^{-1}$). Here, a shift from high to low set voltages with decreasing oxygen flow is evident. Note that for the highest oxidation condition in Figure 5a, a wider set voltage range had to be chosen.

While the set process for the most oxidized sample has a digital character and is characterized by an absence of intermediate resistance steps, the less oxidized samples show more and more intermediate resistance levels close to quantum conductance levels with reducing oxygen content. For the least oxidized sample, an almost gradual set operation behavior characterized by a high number of intermediate resistance levels that can be partly correlated to different quantized conductance levels is obtained. This observation becomes evident by comparing the histograms in Figure 6c,d, which were obtained by analyzing the normalized conductance–voltage curves of Figure 5a,i, respectively, without any data filtering. While for the film grown with 1.0 sccm of oxygen flow only a small peak at 1 $G_0$ is detectable (Figure 6c), numerous quantized conductance states varying from 1 to multiple $G_0$ are evident for the film grown at 0.1 sccm (Figure 6d). Also half-integer states of $G_0$ are detectable, as recently reported for RRAM devices based on hafnium oxide,[20] as well as in a $Cu/Zr_{0.5}Hf_{0.5}O_2/Pt$ ECM device (only in the reset process).[49]

By tuning the oxygen content, the amount of pre-existing oxygen vacancies in the functional layer can be fine-tuned, and by this, the dynamic creation and annihilation process of the conducting filament. By reducing the oxygen contents, the operation voltages can be reduced, and the electric field-driven oxygen migration promoted. This controlled formation of the conductive filament leads to a gradual behavior, especially in the set, but also in the reset process. The resistance moves quasi-continuously on the staircase of dense quantum states, resulting in a gradual character of the set process. Therefore, by oxygen engineering, the switching process can be transitioned between a very abrupt switching characteristic (for the most oxidized case), via a multi-level transition with the accessibility of an additional number of intermediate resistance states (intermediate oxidation conditions), toward a gradual switching characteristic (for the least oxidized films). The situation can be compared to the formation of a conduction band assembled from individual quantum states connected to quantum conduction modes occurring within the filament. The intermediate resistance states can be accessed continuously in the switching operation demonstrated for the least oxidized devices (Figures 5j and 6e).

As mentioned above, a gradual/analog switching behavior is desired for neuromorphic applications to mimic the synaptic behavior of the brain. This behavior is often observed in the reset operation of filamentary-based RRAM devices but scarcely reported for the set operation. Henceforth, the effect of oxygen engineering to facilitate the accessibility of intermediate resistance levels in the set operation is of utmost importance for future device engineering to overcome the so-called von Neumann bottleneck.


© 2020 The Authors. Published by Wiley-VCH GmbH

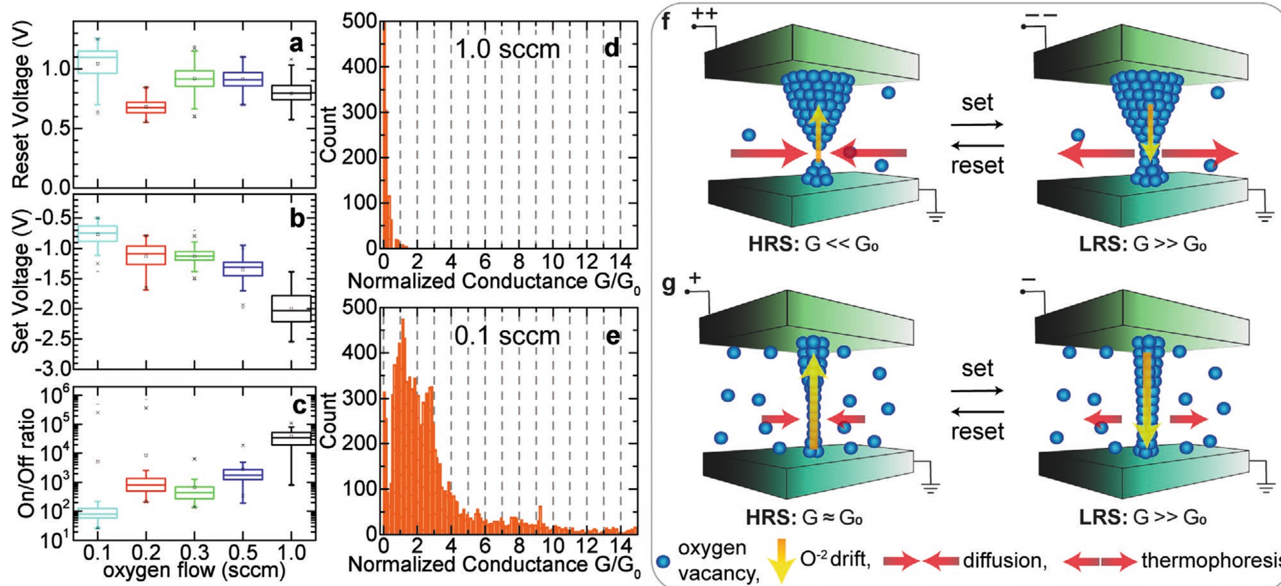


**Figure 6.** Box plots for a) reset and b) set voltages, as well as c) the on/off ratio for all devices under investigation. Reducing the oxygen content by oxygen engineering leads to a decrease in set voltages while the onset of reset voltages seems to slightly increase and the memory window decreases. The decrease in set voltages shows a beneficial effect on the number of quantized conductance steps as can be seen from the difference of the histograms of the d) most oxidized (1.0 sccm) versus the e) least oxidized (0.1 sccm) yttrium oxide-based RRAM device. Schematic representation of the effect of oxygen engineering on the conducting filament morphology for the f) highest and g) lowest oxygen flow. f) In highly oxidized samples, the oxygen vacancies necessary for resistive switching have to be created, thus resulting in high electric fields during the electroforming and set processes. Joule heating-assisted diffusion processes are prominent (red arrows) in addition to electric field induced ionic drift (yellow arrows). g) For oxygen deficiently grown samples with a uniform spatial distribution and high concentration of oxygen vacancies achieved via oxygen engineering, filament formation becomes mainly field driven and only requires the rearrangement of defects as opposed to their creation, lowering forming and set voltages. The high number of defects in the filament vicinity act as acceptors for oxygen during filament growth, thus enabling a higher control during electroforming/set and leading to a lowered power dissipation and to the appearance of quantized conductance levels.

The reset behavior for the most oxidized sample is characterized by a mixture of stepwise and abrupt current drops with a high on/off ratio between the LRS and HRS. Upon decreasing the oxygen content of the yttria films, this abrupt behavior transitions more and more to a gradual/analog crossing, and for oxygen flows below 0.5 sccm the reset behavior is dominated by gradual dynamics. As previously reported, the gradual behavior of the reset and set processes can be utilized for pulse depression and potentiation and also allows for reproducible storage of information in yttrium oxide-based devices.[7] The distribution of the onset of reset voltages is depicted in Figure 6a. The onset of the reset voltage is defined as the voltage at which the resistance of the device is found to decrease within the performed switching operation. As can be seen in the *I–V* curves in Figure 5, the overall reset process, especially when gradual, spans up to 2.5 V. Therefore, it appears that only the onset of the reset process is slightly shifted to higher reset voltages for films with decreased oxygen content.

It has to be mentioned that there is a trade-off between the beneficial effect of oxygen engineering on the operation voltages and the shrinking of the memory window as shown in Figure 6c. The improved heat and electrical conductivity in the devices grown with lower oxygen content results in a shift of the HRS current to higher values while the LRS current remains unchanged, and, as a consequence, the on/off ratio also decreases. However, the LRS and HRS are still clearly distinguishable even in the least oxidized sample, and the overall benefits of oxygen engineering, such as the increased number of accessible intermediate states and reduction of operation voltages, outweigh the drawback of the observed shrinkage of the memory window.

For devices grown with an oxygen flow below 0.5 sccm, the HRS state hardly reaches resistance levels below $G_0^{-1}$ implying an incomplete rupture of the conducting filament in the DC reset process. In this case, the filament only grows/shrinks in lateral size becoming wider/narrower but never being completely ruptured as shown in Figure 6g. This is mainly due to the applied voltage range. Choosing higher reset voltages allows for deeper reset operations but contains the risk of performing a unipolar set operation in the positive voltage polarity. Since no current compliance is applied for the bipolar reset operation, this would result in device hard breakdown. As we have recently reported, deeper resets can be achieved by pulse operation in the nanosecond regime, since the unipolar set operation requires a larger time interval than the bipolar resistive switching operation due to the different underlying switching mechanism.[7]

Again, the observed phenomena can be explained by the effect of oxygen engineering. Thereby, in the growth process, uniformly distributed oxygen vacancies are introduced in the functional dielectric yttrium oxide layer resulting in an increase of the leakage current. These additional defects in the yttrium oxide layer facilitate the formation of the conducting filament. As a result, in contrast to stoichiometric


© 2020 The Authors. Published by Wiley-VCH GmbH

dielectric layers, only a redistribution of pre-existing defects is necessary rather than the creation of new defect states (see Figure 6f vs Figure 6g), which considerably reduces the required forming voltages necessary to create a conducting filament. This implies a reduced power dissipation in the forming process, resulting in a more controllable forming procedure with reduced danger of overvoltage and current overshoots.[50,51] The same concepts can be applied to the observed reduction of the set operation voltages. The increased defect density by oxygen engineering increases the number of defects in the vicinity of the conducting filament facilitating its growth and remarkably reducing the required set voltage (see Figure 6g). Additionally, the increased defect density in oxygen deficient layers and its induced, increased electrical conductivity will be accompanied by an improved thermal conductivity. Thereby, temperature effects in the form of Joule heating are reduced[52] by minimizing competing, temperature assisted driving forces such as Fick's diffusion or Soret's forces (indicated by the smaller red arrows in Figure 6g).[14,53] Both are considered to be the main driving forces in unipolar operated switching devices, which are typically characterized by high on–off ratios, high operation voltages, digital switching behavior, and decreased endurance. Therefore, the minimization of these temperature-assisted processes makes the bipolar resistive switching operation more field driven (yellow arrows in Figure 6f,g), and thus, improves its controllability as underlined by the improved forming voltage and operation voltage distribution. The difference in stoichiometry and the necessary electric field also influences the conducting filament morphology: higher fields result in wider breakdown paths, whereas low electric fields and electric field-driven switching reduces the filament cross-section, enabling improved accessibility of intermediate and quantized conductance states. This behavior can be utilized in pulse operations for depression and potentiation of synaptic weights as previously demonstrated.[7] Additionally, the defect-rich structure of yttrium sesquioxide, which contains natural oxygen vacancy chains along the [110] (or equivalent) direction within its cubic structure, could promote the creation of quantized conduction channels, possibly promoting the improved accessibility of quantized intermediate resistance states.[29]

## 4. Modeling Conductance Quantization Effects

In this section, we attempt to provide an explanation for the observed integer and half-integer conductance values detected in the HRS $I$–$V$ characteristics of our devices as well as for its dispersion around these values. As is well known, conductance levels close to the quantum unit $G_0$ have been reported many times in the past for RS devices.[54,55] This feature has been attributed to the formation of a single or multiple filamentary conducting paths of atomic size cross-section in thin insulating films. The main difficulty for the detection of this quantization effect is the inherent modification of the filamentary path microstructure after each switching cycle. **Figure 7**a illustrates a histogram for the conductance values obtained by considering data from every tenth cycle in the HRS during

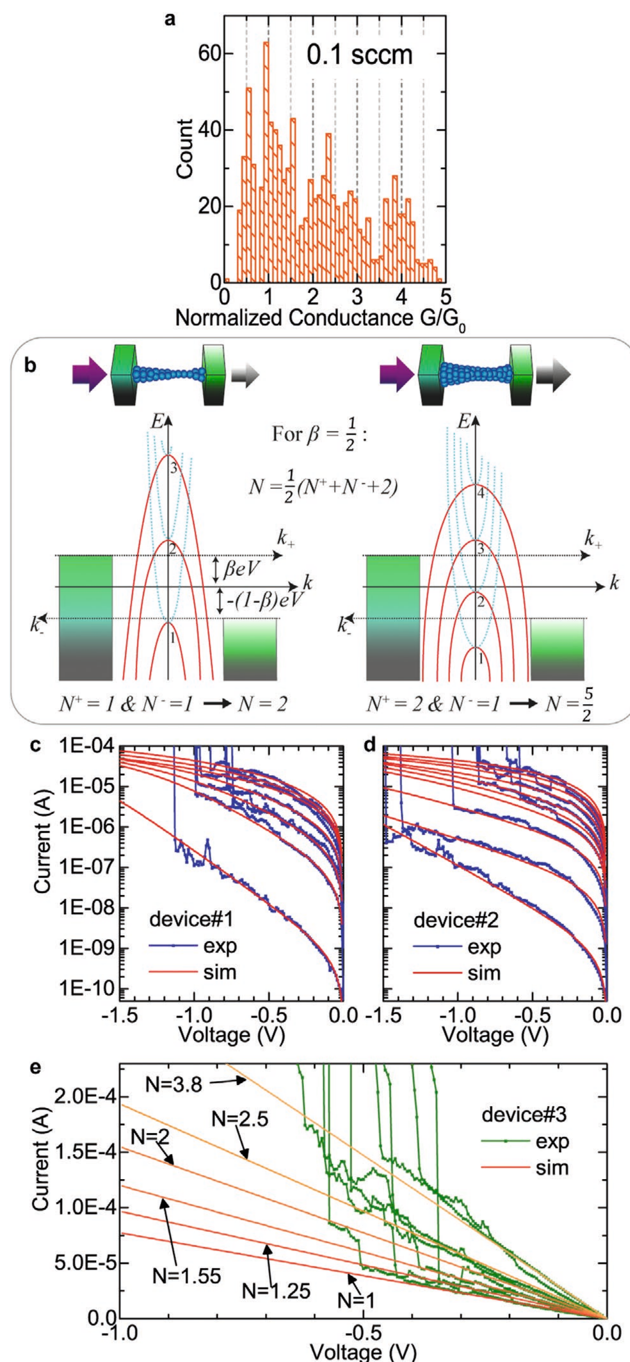


**Figure 7.** a) Histogram of the conductance normalized by the conductance quantum for the same data as presented in e (every tenth cycle, stack with least oxidized $YO_x$, set process). b) Schematic of the sub-bands associated with the constriction. The red solid lines are the longitudinal barrier profiles. The dotted blue lines describe the saddle point potential. $N^+$ and $N^-$ in both examples reflect the number of sub-bands as seen by each reservoir. The simplest case of a symmetrical potential drop distribution ($\beta = ½$) is analyzed for a narrow and wide constriction. c–e) Experimental and simulated charge transport in the set process. c,d) Tunneling through a barrier in the HRS. e) Charge carrier transport through a nanoconstriction which can be simulated with integer and non-integer values of $N$.



© 2020 The Authors. Published by Wiley-VCH GmbH

the set process of 100 consecutive DC cycles carried out in the least oxidized stack (0.1 sccm). Notice that peaks are not only observed at integer values of $G_0$, as expected for the standard Landauer theory,[56] but also at half-integer values of the quantum conductance unit. This is often called nonlinear conductance quantization and has also been reported in the past for RS devices.[57]

More generally, according to Mehonic et al.,[23] the current through these filamentary paths can be expressed as

$$I = NG_0V + f(V) \tag{1}$$

where $N$ is the number of effective conducting channels and $f(V)$ is a nonlinear function that considers the deviation from the original Landauer formula.[18] While the first term in (1) refers to the core region of the filamentary conducting structure, $f$ describes the current contribution associated with uncomplete paths. As reported by Mehonic et al.,[23] $N$ can achieve integer and half-integer values depending on the number of electron transport channels which contribute to the total current taking into account injection from both sides of the structure. In this section, we provide a physics-based expression for this function based on theoretical considerations arising from the physics of mesoscopic conductors. We generalize the analysis to the case of asymmetrical potential drops at the two ends of the constriction and finally we apply it to the investigated devices.

Let $M(E)$ be the distribution of quantized levels within a single constriction as a function of the energy. According to the finite-bias Landauer approach the current associated with the right-going conduction states ($k_+$) reads

$$I^+ = \frac{2e}{h}\int_{-\infty}^{\infty} T(E)M(E)f[E-\beta eV]dE \tag{2}$$

where $T$ is the transmission probability of the structure, $f$ the Fermi–Dirac distribution, and $0 < \beta < 1$ the fraction of the applied voltage that drops at the source side of the constriction (parabolic like shaped as considered in ref. [58]). Assuming zero temperature and treating the first quantized sub-band separately from the rest, $I^+$ reads

$$I^+ \approx \frac{2e}{h}\int_{-\infty}^{\beta eV}\left[\sum_N H(E-\varepsilon_N) + \frac{1}{1+e^{-\alpha(E-\varepsilon_0)}}\right]dE \tag{3}$$

where $\varepsilon_0$ is the energy of the lowest sub-band, $\alpha$ a constant related to the longitudinal curvature of this sub-band, and $\varepsilon_N$ the energy of the sub-bands above $\varepsilon_0$. $H$ is the Heaviside function. By integrating (3), we obtain

$$I^+ \approx \frac{2e^2}{h}\left\{\beta(N^+ + 1)V - \frac{\varepsilon_0}{e} + \frac{1}{e\alpha}ln\left[1+e^{\alpha(\varepsilon_0-\beta eV)}\right]\right\} + C \tag{4}$$

where $N^+$ is the number of sub-bands below the quasi-Fermi level at the cathode. $C$ is an integration constant.

Similarly, for the left-going conduction states ($k_-$), $I^-$ is expressed as

$$I^- = \frac{2e}{h}\int_{-\infty}^{\infty} T(E)M(E)f\left[E+(1-\beta)eV\right]dE \tag{5}$$

Considering, again, the lowest and upper sub-bands separately in the zero temperature limit:

$$I^- \approx \frac{2e}{h}\int_{-\infty}^{-(1-\beta)eV}\left[\sum_N H(E-\varepsilon_N) + \frac{1}{1+e^{-\alpha(E-\varepsilon_0)}}\right]dE \tag{6}$$

which after the integration reads

$$I^- \approx -\frac{2e^2}{h}\left\{(1-\beta)(N^- + 1)V + \frac{\varepsilon_0}{e} - \frac{1}{e\alpha}ln\left[1+e^{\alpha[\varepsilon_0+(1-\beta)eV]}\right]\right\} + C \tag{7}$$

In this case, $N^-$ is the number of sub-bands below the quasi-Fermi level at the anode. $C$ is the same integration constant as in (4).

From (4) and (7), the total current reads

$$I = I^+ - I^- \tag{8}$$

that is,

$$I = \frac{2e^2}{h}\left[\beta(N^+ + 1)V + (1-\beta)(N^- + 1)V + \frac{1}{e\alpha}ln\left(\frac{1+e^{\alpha(\varepsilon_0-\beta eV)}}{1+e^{\alpha[\varepsilon_0+(1-\beta)eV]}}\right)\right] \tag{9}$$

Now, if we define

$$N = \beta(N^+ + 1) + (1-\beta)(N^- + 1) \tag{10}$$

the current reads

$$I = NG_0V + \frac{2e}{h\alpha}ln\left(\frac{1+e^{\alpha(\varepsilon_0-\beta ev)}}{1+e^{\alpha[\varepsilon_0+(1-\beta)eV]}}\right) \tag{11}$$

which is nothing but a generalization of Mehonic's result[23] for the case of asymmetric potential drops at both sides of the constriction. In addition, comparing (1) and (11), we can identify the nonlinear term as

$$f(V) = \frac{2e}{h\alpha}ln\left(\frac{1+e^{\alpha(\varepsilon_0-\beta eV)}}{1+e^{\alpha[\varepsilon_0+(1-\beta)eV]}}\right) \tag{12}$$

Notice that if we consider $\beta$ = ½ and if we disregard the effects of the first tunneling sub-band (this is achieved using $\varepsilon_0 \to -\infty$ in (12)), we recover the celebrated Landauer formula[18] (see Figure 7b). However, as reported in ref. [57], if the difference between $N^+$ and $N^-$ is an odd number, half-integer quantization is obtained, otherwise, $N$ is an integer number. Figure 7c,d shows fitting results corresponding to a pure tunneling process ($N^+ = N^- = 0 \to N = 1$) occurring in two different devices. Notice the good agreement between the experimental and model results. According to the extracted model parameter values,[54] the width of the tunneling barrier is found to be in the range from 1.5 to 13 nm, while the radius of the constriction in the range from 1 to 7 nm, depending on the current magnitude. As the yttrium oxide thickness in the least oxidized devices (0.1 sccm) is 18.88 nm according to the XRR results shown in Table 1, the obtained barrier width values are viable results. For higher currents (i.e.,


© 2020 The Authors. Published by Wiley-VCH GmbH

lower resistance), a larger constriction radius and a lower tunneling barrier is found, which can be interpreted as the stabilization and growth of the filament: with increasing cycle number, the tunneling barrier gradually shrinks, and eventually disappears. At the same time, the conducting filament widens, and, upon closing the tunneling gap, allows for the ballistic transport of electrons manifested in the observation of quantized conductance levels. In the general case, $\beta$ can be different from ½, and consequentially deviations from the expected quantization results are in principle observable. Figure 7e shows results with generalized $N$ numbers. For example, $N = 1.55$ is obtained with $N^+ = 1$, $N^- = 0$, $\beta = 0.55$, and $\varepsilon_0 \rightarrow -\infty$ (no tunneling barrier) and $N = 2.5$ with $N^+ = 2$, $N^- = 1$, $\beta = 0.5$, and $\varepsilon_0 \rightarrow -\infty$. The above results have been obtained with the presumption that current transport takes place exclusively through the nano-constriction and that the contribution from current sneak paths originating from outside the filament can be neglected. However, for devices that show higher leakage currents in the pristine state, an additional term might be required to accurately describe conduction. We find that the obtained simulations are in agreement with the experimental $I$–$V$ curves showing nonlinear conductance quantization. All parameters used for the simulations are listed in Tables S1–S3, Supporting Information.

## 5. Conclusion

In this work, we have shown that the structural and electrical characteristics of yttrium oxide-based RRAM can be finely controlled via oxygen engineering. Structural evaluation through XRD, XRR, and ABF-STEM measurements have revealed that it is possible to fabricate purely cubic *C*-type yttrium oxide while suppressing the monoclinic phase via decreasing the oxygen content of the yttria films. The extracted direct optical bandgaps of the $YO_x$ layers were found to decrease from 5.7 eV by over 0.2 eV to 5.45 eV under less oxidizing conditions. Decreasing the oxygen content of the functional layer reduces the forming and operation voltages, resulting in an overall lowered power dissipation and reduced inter- and intra-device variability. Moreover, by tuning the oxygen content, a digital two-level switching with abrupt set and reset behavior is transitioned to multi-level switching with improved accessibility of intermediate resistance states. These intermediate resistance states show nonlinear conductance quantization, that is, take up integer and non-integer values of the quantum conductance $G_0$, in agreement with a generalized mesoscopic transport model. By further reducing the oxygen content of the yttrium oxide layer, a transition toward a semi-gradual/analog behavior in the reset, as well as in the set operation is achieved. This continuously changing plasticity, accompanied by a very high density of accessible quantized states, makes RRAM based on oxygen engineered yttrium oxide a promising candidate for neuromorphic applications and enables the establishment of high-density multi-bit storage elements.

## 6. Experimental Section

For the structural characterizations, yttrium oxide layers were grown onto *c*-cut sapphire substrates using molecular beam epitaxy (MBE) in a custom designed ultra-high vacuum chamber with a base pressure of $10^{-9}$ mbar. The oxide layers were grown by elemental electron beam evaporation of yttrium. In situ oxidation was achieved by utilizing radio frequency (RF)-activated oxygen radicals from a radical source. A gas purity of 5N for oxygen and 3N (Chempur) for yttrium was chosen to guarantee high purity yttria films. The yttrium oxide layers were grown at 450 °C with a growth rate of either 0.25 or 1.0 Å $s^{-1}$ (for details, see Table 1). The RF power was kept constant at 200 W for all yttria layers, while the oxygen flow was varied from 0.1 up to 1.0 standard cubic centimeter per second (sccm) (see Table 1).

For the fabrication of RRAM devices, the yttrium oxide layers had been grown with the same deposition conditions onto atomic layer deposited electrodes. The layers of bottom electrode were grown onto (100) silicon substrate using sputtering physical vapor deposition (PVD) and then ALD. The PVD layers consisted of 10 nm Ti deposited at 350 °C, then 440 nm AlCu (0.5 at% of Cu) deposited at 450 °C, and 10 nm Ti–80 nm TiN bilayer deposited at 350 °C. The PVD layers were grown in a single run without breaking vacuum. Then, before deposition at 350 °C of the 10 nm ALD TiN electrode, the 80 nm PVD TiN upper layer had been planarized to reduce surface roughness. Finally, 100 nm thick platinum top layers were deposited using a Quorum sputter coater. The Pt top electrodes were patterned using a standard lithography lift-off process, rendering device sizes of 30 × 30 μ$m^2$. XRD and XRR were performed with Cu $K_\alpha$ radiation using a Rigaku SmartLab diffractometer in parallel beam geometry.

XPS was performed using monochromatic Al $K_\alpha$ radiation in a PHI Versaprobe 5000 spectrometer. UV/vis transmission measurements were carried out with an Agilent Cary 7000 Universal Measurement Spectrophotometer in a wavelength range from 2500 to 200 nm. For the electrical characterization, a Keithley 4200 semiconductor characterization system (SCS) was utilized biasing the platinum top electrode, while keeping the titanium nitride bottom electrode grounded. To prevent device hard breakdown, the internal current compliance of the Keithley SCS had been used.

ABF-STEM as well as EELS measurements were performed using a JEOL JEM-ARM200F operated at 120 kV. ABF images were acquired by using the JEOL BF detector with a 3 mm BF aperture and an inserted beam stopper. The EEL spectra were acquired with a Gatan Enfina with the entry aperture set to 1 mm. The EEL spectra were integrated over the yttria layer thickness and the background spectra were subtracted with HyperSpy software.[59] For the multislice simulations with Dr. Probe software, a voltage of 120 kV, an aperture radius $\alpha$ of 25 mrad, a probe size of 0.08 nm and an ABF detector with 10–30 mrad detection range were used. The microscope aberrations were set to zero. The multislice data was generated with equidistant slicing and a thickness of ≈10 nm. TEM sample preparation was performed with a JEOL JIB-4600F focused ion beam system.

## Supporting Information

Supporting Information is available from the Wiley Online Library or from the author.

## Acknowledgements

The work leading to this publication has been undertaken in the framework of the WAKeMeUP project which received funding from the Electronic Components and Systems for European Leadership Joint Undertaking in collaboration with the European Union's H2020 Framework Programme (H2020/2014-2020) and National Authorities, under grant agreement no 783176. Funding by the Auvergne-Rhône Alpes Region and the Federal Ministry of Education and Research (BMBF) under contract 16ESE0298 are gratefully acknowledged. E.P. acknowledges funding from the Deutscher Akademischer Austauschdienst (DAAD). This work was supported by the Deutsche


© 2020 The Authors. Published by Wiley-VCH GmbH

Forschungsgemeinschaft under project AL 560/13-2. Also, funding from DFG grant under project number 384682067, MO 3010/3-1, and AL 560/21-1, and the European Research Council (ERC) "Horizon 2020" Program under grant no. 805359-FOXON are gratefully acknowledged. E.M. also acknowledges the funding from the WAKeMeUP project as well as the support from the Ministerio de Ciencia, Innovación y Universidades, Spain (TEC2017-84321-C4-4-R and PCI2018-093107). Thanks to Katrin Walter for carrying out the UV/vis measurements and to Seyma Topcu for obtaining the current–voltage curves. S.P. and E.P. have equally contributed to the paper.

Open access funding enabled and organized by Projekt DEAL.

## Conflict of Interest

The authors declare no conflict of interest.

## Keywords

analog, conductance quantization, gradual, neuromorphic, oxygen engineering, resistive switching memory, yttria, yttrium oxide

Received: April 27, 2020
Revised: June 12, 2020
Published online: September 9, 2020

[1] A. C. Torrezan, J. P. Strachan, G. Medeiros-Ribeiro, R. S. Williams, *Nanotechnology* **2011**, *22*, 485203.
[2] D. J. Wouters, R. Waser, M. Wuttig, *Proc. IEEE* **2015**, *103*, 1274.
[3] S. Kumar, Z. Wang, X. Huang, N. Kumari, N. Davila, J. P. Strachan, D. Vine, A. L. D. Kilcoyne, Y. Nishi, R. S. Williams, *Appl. Phys. Lett.* **2017**, *110*, 103503.
[4] S. Petzold, S. U. Sharath, J. Lemke, E. Hildebrandt, C. Trautmann, L. Alff, C. Wenger, L. Alff, *IEEE Trans. Nucl. Sci.* **2019**, *66*, 1715.
[5] Z. Zhang, Y. Wu, H.-P. Wong, S. S. Wong, *IEEE Electron Device Lett.* **2013**, *34*, 1005.
[6] R. Waser, R. Dittmann, G. Staikov, K. Szot, *Adv. Mater.* **2009**, *21*, 2632.
[7] S. Petzold, E. Piros, S. U. Sharath, A. Zintler, E. Hildebrandt, L. Molina-Luna, C. Wenger, L. Alff, *Semicond. Sci. Technol.* **2019**, *34*, 075008.
[8] S. U. Sharath, M. J. Joseph, S. Vogel, E. Hildebrandt, P. Komissinskiy, J. Kurian, T. Schroeder, L. Alff, *Appl. Phys. Lett.* **2016**, *109*, 173503.
[9] R. Waser, M. Aono, in *Nanoscience and Technology* (Ed: P. Rodgers), Nature Publishing Group, UK **2009**, pp. 158–165.
[10] M. Lanza, *Materials* **2014**, *7*, 2155.
[11] F. Pan, S. Gao, C. Chen, C. Song, F. Zeng, *Mater. Sci. Eng. R Rep.* **2014**, *83*, 1.
[12] D. Ielmini, *Semicond. Sci. Technol.* **2016**, *31*, 063002.
[13] S. Gao, X. Yi, J. Shang, G. Liu, R.-W. Li, *Chem. Soc. Rev.* **2019**, *48*, 1531.
[14] S. Kumar, C. E. Graves, J. P. Strachan, E. M. Grafals, A. L. D. Kilcoyne, T. Tyliszczak, J. N. Weker, Y. Nishi, R. S. Williams, *Adv. Mater.* **2016**, *28*, 2772.
[15] A. Zintler, U. Kunz, Y. Pivak, S. U. Sharath, S. Vogel, E. Hildebrandt, H.-J. Kleebe, L. Alff, L. Molina-Luna, *Ultramicroscopy* **2017**, *181*, 144.
[16] K.-H. Xue, X.-S. Miao, *J. Appl. Phys.* **2018**, *123*, 161505.
[17] S. Petzold, E. Miranda, S. U. Sharath, J. Muñoz-Gorriz, T. Vogel, E. Piros, N. Kaiser, R. Eilhardt, A. Zintler, L. Molina-Luna, J. Suñé, L. Alff, *J. Appl. Phys.* **2019**, *125*, 234503.
[18] R. Landauer, *IBM J. Res. Dev.* **1957**, *1*, 223.
[19] X. Zhu, W. Su, Y. Liu, B. Hu, L. Pan, W. Lu, J. Zhang, R.-W. Li, *Adv. Mater.* **2012**, *24*, 3941.
[20] S. U. Sharath, S. Vogel, L. Molina-Luna, E. Hildebrandt, C. Wenger, J. Kurian, M. Duerrschnabel, T. Niermann, G. Niu, P. Calka, M. Lehmann, H.-J. Kleebe, T. Schroeder, L. Alff, *Adv. Funct. Mater.* **2017**, *27*, 1700432.
[21] S. Gao, F. Zeng, C. Chen, G. Tang, Y. Lin, Z. Zheng, C. Song, F. Pan, *Nanotechnology* **2013**, *24*, 335201.
[22] W. Xue, Y. Li, G. Liu, Z. Wang, W. Xiao, K. Jiang, Z. Zhong, S. Gao, J. Ding, X. Miao, X.-H. Xu, R.-W. Li, *Adv. Electron. Mater.* **2020**, *6*, 1901055.
[23] A. Mehonic, A. Vrajitoarea, S. Cueff, S. Hudziak, H. Howe, C. Labbé, R. Rizk, M. Pepper, A. J. Kenyon, *Sci. Rep.* **2013**, *3*, 2708.
[24] B. Rajendran, Y. Liu, J. Seo, K. Gopalakrishnan, L. Chang, D. J. Friedman, M. B. Ritter, *IEEE Trans. Electron Devices* **2013**, *60*, 246.
[25] X. Yan, J. Zhao, S. Liu, Z. Zhou, Q. Liu, J. Chen, X. Y. Liu, *Adv. Funct. Mater.* **2018**, *28*, 1705320.
[26] X. Yan, Q. Zhao, A. P. Chen, J. Zhao, Z. Zhou, J. Wang, H. Wang, L. Zhang, X. Li, Z. Xiao, K. Wang, C. Qin, G. Wang, Y. Pei, H. Li, D. Ren, J. Chen, Q. Liu, *Small* **2019**, *15*, 1901423.
[27] R. Guo, W. Lin, X. Yan, T. Venkatesan, J. Chen, *Appl. Phys. Rev.* **2020**, *7*, 011304.
[28] X. Yan, L. Zhang, H. Chen, X. Li, J. Wang, Q. Liu, C. Lu, J. Chen, H. Wu, P. Zhou, *Adv. Funct. Mater.* **2018**, *28*, 1803728.
[29] K. Z. Rushchanskii, S. Blügel, M. Ležaić, *Faraday Discuss.* **2019**, *213*, 321.
[30] K. Onisawa, M. Fuyama, K. Tamura, K. Taguchi, T. Nakayama, Y. A. Ono, *J. Appl. Phys.* **1990**, *68*, 719.
[31] P. Lei, W. Leroy, B. Dai, J. Zhu, X. Chen, J. Han, D. Depla, *Surf. Coat. Technol.* **2015**, *276*, 39.
[32] J. Leng, Z. Yu, Y. Li, D. Zhang, X. Liao, W. Xue, *Appl. Surf. Sci.* **2010**, *256*, 5832.
[33] M. Mishra, P. Kuppusami, T. N. Sairam, A. Singh, E. Mohandas, *Appl. Surf. Sci.* **2011**, *257*, 7665.
[34] P. Zaumseil, *RCRefSim: Rocking Curve and Reflectivity Simulation,* IHP, Frankfurt (Oder), Germany **2005**.
[35] J. Barthel, *Ultramicroscopy* **2018**, *193*, 1.
[36] A. Travlos, N. Boukos, G. Apostolopoulos, A. Dimoulas, C. Giannakopoulos, *Mater. Sci. Eng. B* **2004**, *109*, 52.
[37] C. Pi, Y. Ren, Z. Q. Liu, W. K. Chim, *Electrochem. Solid-State Lett.* **2012**, *15*, G5.
[38] P. Malacrida, H. G. S. Casalongue, F. Masini, S. Kaya, P. Hernández-Fernández, D. Deiana, H. Ogasawara, I. E. L. Stephens, A. Nilsson, I. Chorkendorff, *Phys. Chem. Chem. Phys.* **2015**, *17*, 28121.
[39] R. M. Jafer, E. Coetsee, A. Yousif, R. E. Kroon, O. M. Ntwaeaborwa, H. C. Swart, *Appl. Surf. Sci.* **2015**, *332*, 198.
[40] Y. C. Jung, S. Seong, T. Lee, I.-S. Park, J. Ahn, *J. Nanosci. Nanotechnol.* **2015**, *15*, 7586.
[41] I.-S. Park, Y. C. Jung, S. Seong, J. Ahn, J. Kang, W. Noh, C. Lansalot-Matras, *J. Mater. Chem. C* **2014**, *2*, 9240.
[42] F. Jollet, C. Noguera, N. Thromat, M. Gautier, J. P. Duraud, *Phys. Rev. B* **1990**, *42*, 7587.
[43] J. X. Zheng, G. Ceder, T. Maxisch, W. K. Chim, W. K. Choi, *Phys. Rev. B* **2006**, *73*, 104101.
[44] N. Raghavan, *Microelectron. Reliab.* **2014**, *54*, 2253.
[45] X. Yan, Y. Li, J. Zhao, Y. Li, G. Bai, S. Zhu, *Appl. Phys. Lett.* **2016**, *108*, 033108.
[46] S. Petzold, A. Zintler, R. Eilhardt, E. Piros, N. Kaiser, S. U. Sharath, T. Vogel, M. Major, K. P. McKenna, L. Molina-Luna, L. Alff, *Adv. Electron. Mater.* **2019**, *5*, 1900484.
[47] X. B. Yan, Y. D. Xia, H. N. Xu, X. Gao, H. T. Li, R. Li, J. Yin, Z. G. Liu, *Appl. Phys. Lett.* **2010**, *97*, 112101.
[48] G. Niu, P. Calka, P. Huang, S. U. Sharath, S. Petzold, A. Gloskovskii, K. Fröhlich, Y. Zhao, J. Kang, M. A. Schubert, F. Bärwolf, W. Ren, Z.-G. Ye, E. Perez, C. Wenger, L. Alff, T. Schroeder, *Mater. Res. Lett.* **2019**, *7*, 117.

 © 2020 The Authors. Published by Wiley-VCH GmbH

[49] J. Zhao, Z. Zhou, Y. Zhang, J. Wang, L. Zhang, X. Li, M. Zhao, H. Wang, Y. Pei, Q. Zhao, Z. Xiao, K. Wang, C. Qin, G. Wang, H. Li, B. Ding, F. Yan, K. Wang, D. Ren, B. Liu, X. Yan, *J. Mater. Chem. C* **2019**, *7*, 1298.
[50] H. J. Wan, P. Zhou, L. Ye, Y. Y. Lin, T. A. Tang, H. M. Wu, M. H. Chi, *IEEE Electron Device Lett.* **2010**, *31*, 246.
[51] Y.-S. Chen, W.-H. Liu, H.-Y. Lee, P.-S. Chen, S.-M. Wang, C.-H. Tsai, Y.-Y. Hsu, P.-Y. Gu, W.-S. Chen, F. Chen, C.-H. Lien, M.-J. Tsai, *Proc. 2011 Int. Symp. VLSI Technol. Syst. Appl.* **2011**, 1.
[52] A. Rodriguez-Fernandez, J. Muñoz-Gorriz, J. Suñé, E. Miranda, *Microelectron. Reliab.* **2018**, *88–90*, 142.
[53] J. J. Yang, D. B. Strukov, D. R. Stewart, *Nat. Nanotechnol.* **2013**, *8*, 13.
[54] E. A. Miranda, C. Walczyk, C. Wenger, T. Schroeder, *IEEE Electron Device Lett.* **2010**, *31*, 609.
[55] Y. Li, S. Long, Y. Liu, C. Hu, J. Teng, Q. Liu, H. Lv, J. Suñé, M. Liu, *Nanoscale Res. Lett.* **2015**, *10*, 420.
[56] S. Datta, *Electronic Transport in Mesoscopic Systems*, Cambridge University Press, New Delhi **1997**.
[57] E. Miranda, S. Kano, C. Dou, K. Kakushima, J. Suñé, H. Iwai, *Appl. Phys. Lett.* **2012**, *101*, 012910.
[58] E. Miranda, J. Suñé, *Microelectron. Reliab.* **2004**, *44*, 1.
[59] F. de la Peña, E. Prestat, V. T. Fauske, P. Burdet, P. Jokubauskas, M. Nord, T. Ostasevicius, K. E. MacArthur, M. Sarahan, D. N. Johnstone, J. Taillon, J. Lähnemann, V. Migunov, A. Eljarrat, J. Caron, T. Aarholt, S. Mazzucco, M. Walls, T. Slater, F. Winkler, pquinn-dls, B. Martineau, G. Donval, R. McLeod, E. R. Hoglund, I. Alxneit, D. Lundeby, T. Henninen, L. F. Zagonel, A. Garmannslund, *Hyperspy/Hyperspy: HyperSpy v1.5.2*, Zenodo **2019**.





© 2020 The Authors. Published by Wiley-VCH GmbH